

# Geophysical Research Letters

## RESEARCH LETTER

10.1029/2020GL087786

### Key Points:

- We perform the joint analysis of deformation and gravity data encompassing the December 2018 eruption of Etna
- Time series from superconducting gravimeters are used to gain insight into the processes associated with a volcanic eruption
- A complex mechanism led to the eruption, involving inelastic accommodation of the strain and formation of dry fractures

### Supporting Information:

- Supporting Information S1

### Correspondence to:

F. Cannavò,  
flavio.cannavo@ingv.it

### Citation:

Chauhan, M. S., Cannavò, F., Carbone, D., & Greco, F. (2020). Insights into Mount Etna December 2018 eruption from joint inversion of deformation and gravity data. *Geophysical Research Letters*, 47, e2020GL087786. <https://doi.org/10.1029/2020GL087786>

Received 3 MAR 2020

Accepted 2 AUG 2020

Accepted article online 10 AUG 2020

## Insights Into Mount Etna December 2018 Eruption From Joint Inversion of Deformation and Gravity Data

Mahak Singh Chauhan<sup>1</sup> , Flavio Cannavò<sup>1</sup> , Daniele Carbone<sup>1</sup> , and Filippo Greco<sup>1</sup> 

<sup>1</sup>Istituto Nazionale di Geofisica e Vulcanologia, Sezione di Catania-Osservatorio Etneo, Catania, Italy

**Abstract** We present results of the joint analysis of ground deformation and superconducting gravity data encompassing Etna's December 2018 eruption. The horizontal ground deformation points to a mechanism of dike opening. Accordingly, we consider forward analytical models describing the effects of a tensile dislocation and use two data inversion approaches, based on heuristic and probabilistic methods. The observed changes can be explained assuming the intrusion of a fluid lighter than bubble-free magma, along a dike-like structure. However, the poor fit to the vertical deformation and the discrepancy between bulk volume increase, deduced by the data inversion (some tens of millions of m<sup>3</sup>), and volume emitted through effusive activity ( $\sim 1 \times 10^6$  m<sup>3</sup>) suggest that a more complex mechanism led to the eruption, involving partial inelastic accommodation of the strain and the formation of void space through increase in the fracturing rate of the medium.

**Plain Language Summary** Volcanic eruptive activity is often preceded and accompanied by ground deformation and changes in the local gravity field, in turn driven by the dynamics of magma in the plumbing system of the volcano. The analysis of deformation and gravity data can provide unique information on intrusive events leading to paroxysmal activity. Here, we use ground deformation and gravity data to shed new light on the December 2018 eruption of Etna, which ensued from fissures in the upper SE flank of the volcano. Data inversion indicates that the eruption was fed by the intrusion of light magma along a sheet-like structure, cutting the SE sector of the volcanic edifice. However, some features of the available observations suggest that the mechanism, which led to the eruptive event involved, besides the elastic deformation of the volcanic edifice in response to the magma intrusion, inelastic accommodation of the strain, and formation of dry fractures.

## 1. Introduction

Mount Etna is one of the most active and better monitored volcanoes in the world (Cannavò et al., 2017; Carbone et al., 2019; Di Grazia et al., 2009). Its monitoring system, managed by the INGV Catania Section-Osservatorio Etneo, includes ~160 multiparameter permanent stations, clustered on the volcano summit and flanks (<https://www.ct.ingv.it/index.php/monitoraggio-e-sorveglianza/mappa-stazioni-ingv-oe>). This large amount of sensors allows us to gather many pieces of information on the processes driving the eruptive activity.

Among the recent eruptions of Mount Etna, the most significant is the one that started on the morning of 24 December 2018. This event was preceded by two years of ground uplift at a nearly constant rate (Cannavò et al., 2019) and by increasing explosive and effusive activity at the summit craters during the last few months before the main eruption (Cannavò, 2019; Laiolo et al., 2019). A seismic swarm of low-magnitude volcano-tectonic events, located in a shallow volume (1–2 km) beneath the southeastern flank of the volcano, was recorded since 8:30 UTC of 24 December (Alparone et al., 2020). More than 1 hr later, the summit GPS stations started to record a coherent pattern of ground deformation (Cannavò, 2019). The ground displacement reached its apex between 11:00 and 12:00 UTC, when a 2 km long eruptive fissure opened at the base of the New South-East Crater and along the western flank of the Valle del Bove (Bonforte et al., 2019; Figure 1). Strong Strombolian activity and several lava flows occurred along the eruptive fissure (Laiolo et al., 2019). An intense seismic swarm accompanied the eruptive activity; it involved different volcano-tectonic structures on the flanks of the volcano and culminated in the 26 December Mw 4.9 earthquake (Bonforte et al., 2019; De Novellis et al., 2019). Activity along the eruptive fissure lasted until 27 December. Based on MODIS and SENTINEL 2 images, Laiolo et al. (2019) estimated a total volume

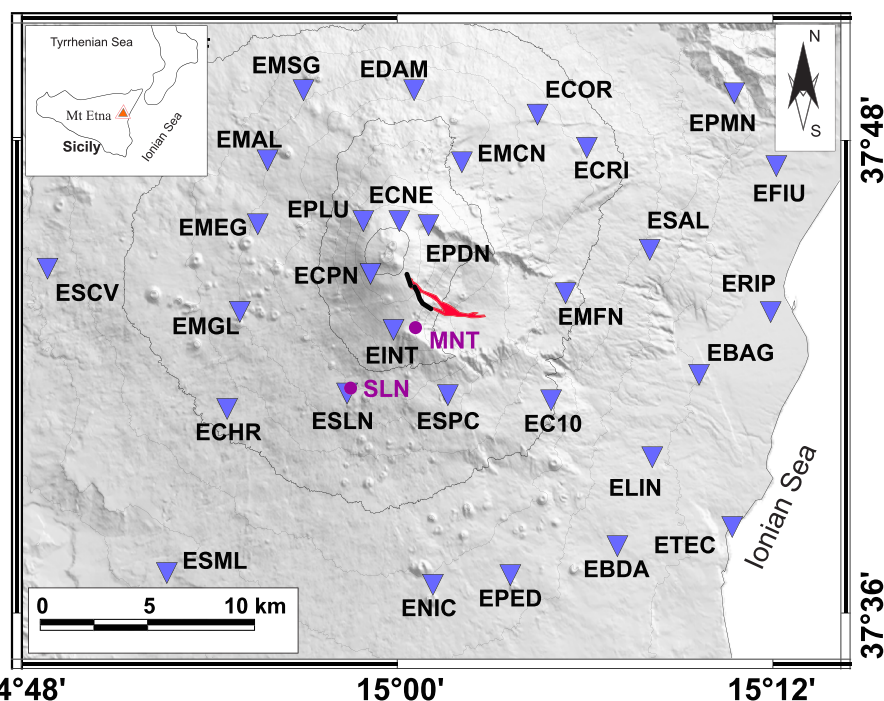


**Figure 1.** Sketch map of Mount Etna showing position of the GPS (blue triangles) and gravity (magenta dots) stations in the permanent INGV-OE monitoring network. The position of the eruptive fissure of the December 2018 eruption (thick black line) and the lava field (red area) are also indicated.

emitted through effusive activity slightly less than  $1 \times 10^6 \text{ m}^3$ , while a larger total emitted dense-rock equivalent volume ( $\sim 2.5 \times 10^6 \text{ m}^3$ ) has been estimated through remote sensing (Calvari et al., 2020).

Here we shed new light on the mechanism behind the December 2018 eruption through the joint analysis of GPS and gravity data. The availability of high-precision continuous data from superconducting gravimeters (SGs) allows us, for the first time, to use the short-term and relatively low-amplitude gravity signature of a fast intrusive event for retrieving details on the characteristics of the driving processes. Indeed, gravity changes as the ones presented here could not be observed through the more conventional spring-type instruments and more widely performed campaign-style measurements (Carbone et al., 2017).

## 2. Data and Methodology

Etna's permanent GPS network has been running since 2000; it now consists of 39 stations across the whole volcano edifice (Figure 1). Raw GPS data are recorded through Leica Geosystems instruments and processed on a daily basis, using the GAMIT/GLOBK software (Dong et al., 1998; Herring et al., 2010; King & Bock, 2004). The processed GPS solutions are referred to the geodetic reference frame, specifically designed for the Etnaean area (see also Text S1 in the supporting information; Altamimi et al., 2016; Bruno et al., 2012; Palano et al., 2010, 2017).

The deformation field induced by the December 2018 intrusive event was computed as the change in static position of each GPS station between 23 and 26 December. The displacement field (Figure 2a) was computed using 30 three-dimensional vectors. In the near field, the horizontal component of the displacement field shows the characteristic pattern associated to dike opening, with predominant displacements almost orthogonal to the strike of the dike.

A mini-array of three GWR iGrav SGs (Warburton et al., 2010) was installed on Etna between September 2014 and July 2016 (Carbone et al., 2019). This is the first network of SGs ever installed on an active volcano. During the interval under consideration in the present study, only two iGrav in the Etna mini-array were operating, one in the facilities of the Serra La Nave Astrophysical Observatory (SLN), the other at

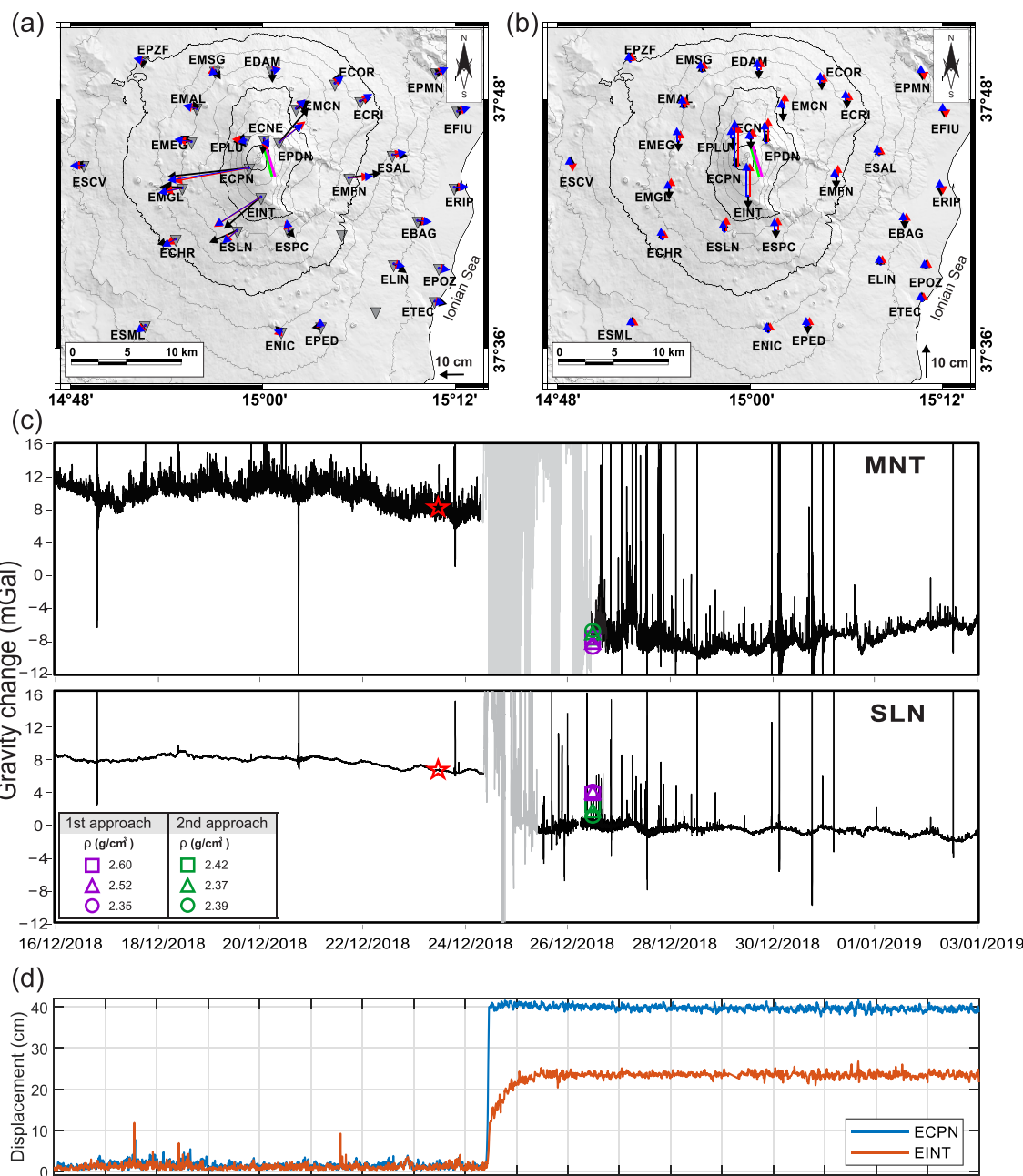


**Figure 2.** (a) Observed (black arrows) and calculated (red arrows = first PSA approach  $w_{III}$ ; blue arrows = second PSA approach  $w'_{III}$ ) horizontal components of the deformation field during the 23–26 December 2018 interval. (b) Same as (a), but for the vertical component of the deformation field. (c) Gravity time series from MNT (top) and SLN (bottom) stations. The light gray parts in the two time series are not reliable, due to the strong instrumental noise during the paroxysmal phase of the eruption. In both panels, symbols indicate gravity changes resulting from the two PSA inversion approaches (changes with respect to the reference symbol, that is, the red star). (d) GPS time series (horizontal strength) recorded at ECPN and EINT stations.

Montagnola hut (MNT; Figure 1). The average noise level at SLN is only slightly higher than that observed in nonvolcanic sites, while at MNT, due to the higher level of volcano-related seismic noise, the noise level is up to 15 times higher than at SLN, over the frequency band of 10 mHz to 0.1 Hz (Carbone et al., 2019). Over longer timescales (minutes to years), SGs supply higher-quality data than the more widely used spring gravimeters, since they are free from instrumental drift and artifacts driven by ambient parameters (Carbone et al., 2017).

The gravity change at both MNT and SLN across the December 2018 eruption is evaluated as the change in the average level of the signal before and after the phase of strong high-frequency noise accompanying the eruptive event (gray parts of the time series in Figure 2c). Indeed, instrumental effects induced by strong volcanic tremor (Carbone et al., 2019) prevent information about the local changes in gravity acceleration from being retrieved at MNT and SLN during, respectively, 08:00 of 24 December to 06:00 of 26 December and 08:00 of 24 December to 11:00 of 25 December (Figure 2c). Gravity decreases with amplitude of 16 and 7  $\mu\text{Gal}$  were observed at MNT and SLN, respectively, across the eruptive event.

To get new insight into the source process behind the December 2018 eruption of Mount Etna, we jointly exploit the information coming from ground deformation and gravity data. The features of the deformation field associated with the eruption (section 1 and Figure 2a) lead us to choose the sets of analytical expressions by Okada (1992) and Okubo (1992). Both analytical formulations allow the calculation of the effects arising from a tensile dike-like structure buried in a homogeneous half-space, and while the former allows calculating the ground deformation due to the tensile stress, the latter allows calculating the corresponding gravity change. The Okada and Okubo analytical formulations share the same input (geometrical) parameters, with the only difference that the Okubo model also requires the density of host rock and intruding material to be supplied as inputs. It is important to stress that, contrarily to previous studies, based on INSAR data (Bonforte et al., 2019; De Novellis et al., 2019), where more complex modeling frameworks were considered (composite dike models), here we prefer to utilize a single model source. Indeed, the above studies focus on a relatively long interval (6 days), that is constrained by the acquisition dates of two consecutive interferograms (22 and 28 December), implying that, besides the tensile dislocation due to the intrusion of the feeder dike, they address other (second order) deformation effects.

To perform the data inversion and estimate the model parameters, we define the objective function in terms of weighted mean of squared residuals (Cannavò, 2019):

$$e = \frac{1}{N} \sum_{i=1}^{N_s} \sum_{j=1}^{N_{c_i}} \frac{|(d_{ij} - d'_{ij})w_i|^2}{\sigma_{ij}^2}, \quad (1)$$

where  $N_{c_i}$  is the number of data components measured at the  $i$ th sensor (e.g., 3 for vectors of displacement measured at GPS stations),  $N = \sum_{i=1}^{N_s} N_{c_i}$  is the total number of available data from all the sensors ( $N_s$ ),  $d_{ij}$  and  $d'_{ij}$  are the observed and predicted data, respectively,  $\sigma_{ij}$  is the standard error associated with each data point (on average,  $\sim 1$  and  $\sim 3$  cm for, respectively, the horizontal and vertical components of GPS data;  $\sim 1 \mu\text{Gal}$  for gravity data), and  $w_i$  is the weight assigned to the each observation point. The goal is to find a source model able to minimize the objective function (Equation 1). In the case of a joint inversion, the data vector represents the combined data set. Since gravity data from only two observation points are available, while GPS data are available from as many as 30 three-component stations, special care needs to be paid when defining the weights ( $w_i$ ) in the objective function. The joint inversion of the two data sets was performed through minimization of the reduced chi-square statistic, normalized for the number of samples for each data type. This allows obtaining comparable contributions from data sets with different numbers of observations.

To jointly invert the available GPS and gravity data set, we use two techniques, one based on the Pattern Search Algorithm (PSA; Audet & Dennis, 2002), the other based on a probabilistic approach through the Bayesian Markov Chain Monte Carlo (MCMC) method (Hastings, 1970). The PSA is a heuristic optimization technique that does not require the gradient of the objective function to retrieve the parameters of the searched model. The PSA algorithm iteratively generates an adaptive grid of model parameters; the inversion process aims to find the model parameters that allow minimizing the misfit defined in Equation 1. The selected model is thus the one that allows the best possible fit between observed and synthetic data. The application of the PSA method allows obtaining only the best model in terms of misfit, without any insight on the characteristics of the uncertainty affecting each model parameter. The latter can be retrieved through application of the probabilistic methods.

Through the probabilistic approach, we can calculate the posterior probability distribution of the model parameters  $\mathbf{m}$ , according to the Bayes's theorem (Tarantola, 1984):

$$p(\mathbf{m}|\mathbf{d}) = \frac{p(\mathbf{d}|\mathbf{m})p(\mathbf{m})}{p(\mathbf{d})}, \quad (2)$$

where  $p(\mathbf{d}|\mathbf{m})$  is the likelihood function of  $\mathbf{m}$ , given the data  $\mathbf{d}$ ,  $p(\mathbf{m})$  is the prior distribution and  $p(\mathbf{d})$  is the normalizing factor, called the marginal likelihood (Sen & Stoffa, 1996; Tarantola & Valette, 1982). For the data vector  $\mathbf{d}$  and associated uncorrelated error ( $\sigma$ ), we can write the likelihood function as follows:

$$p(\mathbf{d}|\mathbf{m}) = (2\pi)^{-N/2} |\Sigma|^{-1/2} \exp\left(\left[\frac{-1}{2} \mathbf{r}^T \Sigma^{-1} \mathbf{r}\right]\right), \quad (3)$$

where  $\mathbf{r}$  is the residual vector ( $d - d'$ ) and  $\Sigma \in N(0, \sigma_{ij}^2/w_i)$  is the diagonal weighted covariance matrix.

The posterior probability distribution (Equation 2) can be sampled through the MCMC algorithm, which incorporates the Metropolis-Hastings algorithm (Hastings, 1970; Mosegaard & Tarantola, 1995) and allows obtaining a sequence of random samples using Equation 2. For any accepted current model  $m_{current}$ , the algorithm draws a new sample randomly from the prior probability density distribution (uniform in our case), in order to retrieve a new trial model, thus exploring the model parameter space. The acceptance of the trial sample is based on the ratio of the likelihoods (Equation 3) of two samples ( $p_{trial}/p_{current}$ ). The trial sample is accepted as a sample of the posterior density distribution if the ratio is greater than a random value drawn between 0 and 1 (Amey et al., 2018; Minson et al., 2013). The algorithm is tuned during the initial burn-in stage, in order to achieve an optimal acceptance rate (i.e., the ratio between the accepted samples and the total probed samples) (~15–25%) and only post burn-in samples are considered representative samples of the posterior distribution (Bagnardi & Hooper, 2018). Any statistic computed on this set of samples is our best guess of the same statistic on the true posterior distribution  $p(\mathbf{m}|\mathbf{d})$ .

### 3. Results

#### 3.1. PSA Inversion

The joint inversion of the deformation and gravity data based on PSA is performed following two different approaches.

Under the former approach, we first invert the deformation field, to obtain the geometrical parameters of the source structure that best fits the observed displacement data (Figures 2a and 2b). As a second step, we fix the retrieved geometry and invert the gravity data to find the best fitting density of the intrusive body.

Results from the application of the first approach are shown in Table 1—lines  $w_I - w_{III}$ —and Figures 2a–2c (purple symbols). If the same weight is set for all the available input parameters (Table 1 line  $w_I$ ), the density value resulting from the calculation allows explaining the gravity change observed at MNT, while the amplitude of the calculated gravity change at SLN is much lower than observed (purple square symbol in panel c of Figure 2). Even if the weight assigned to the gravity datum from SLN is increased in the inversion (Table 1; lines  $w_{II}$  and  $w_{III}$ ), it is not possible to obtain an adequate fit of the observed gravity change, while keeping the geometrical parameters of the intrusive body fixed (purple triangle and circle symbols in Figure 2c).

Under the second approach, a simultaneous inversion of deformation and gravity data is performed through the PSA. First, the same weight is given to all the available input data (Table 1, line  $w'_I$ ). The resulting best fitting density and calculated gravity values are close to those obtained through the previous approach (green square symbol in panel b of Figure 2). To improve the fit of calculated to observed gravity data, we tune the weights of the gravity observations from both MNT and SLN (Table 1, lines  $w'_{II}$  and  $w'_{III}$ ). A satisfactory fit is eventually achieved for both deformation (Figures 2a and 2b) and gravity (green triangle and circle symbols Figure 2c) data.

Comparison of the results obtained following the two approaches shows that the strongest differences in the best fitting parameters occur for the size (mostly width) of the source structure. This difference indicates that, to explain the gravity decrease observed at SLN, the source structure must be rooted deeper in the feeding system of Etna, compared to models that match the other parameters (see results obtained through the first approach).

**Table 1**  
*Model Parameters Calculated Through the Inversion Methods Described in the Text*

Parameters (unit)	East (m)	North (m)	Depth (m)	Azimuth (°)	Dip (°)	Length (m)	Width (m)	Tensile (m)	Density (g/cm <sup>3</sup> )	Weights (MNT, SLN)	RMS error
Lower bounds	481,478	4,172,831	-10,000	0	0	100	100	0	0	0	
Upper Bounds	521,478	4,181,831	1,500	360	90	10,000	10,000	10	3		
1st Approach	PSA	500,903	4,177,003	1,500	163.572	89.9	4,052	3,990	1,072	2.601	$w_I(1,1)$
										2.516	$w_{II}(5, 8)$
										2.352	$w_{III}(5, 12)$
2nd Approach	PSA	500,645	4,176,942	1,500	164.081	89.9	3,894	5,024	1,070	2.415	$w'_I(3, 5)$
		500,620	4,176,896	1,500	164.028	89.4	3,747	5,847	1,081	2.368	$w'_{II}(5, 8)$
	Bayesian	500,636 ± 202	4,176,902 ± 150	1,490 ± 10	162.46 ± 1.0	87.5 ± 1.6	3,601 ± 404	6,462 ± 436	1,108 ± 0.17	2,408 ± 0.11	$w'_{III}$

Note. The first two rows show the boundaries of the search ranges. The first approach involves (i) inverting the deformation field to obtain the geometrical parameters of the “best source” and (ii) fixing the retrieved geometry and inverting the gravity data to find the density of the intrusive body. The second approach involves the joint inversion of deformation and gravity data. The depth refers to the top of the dike and is positive upward from the reference level.

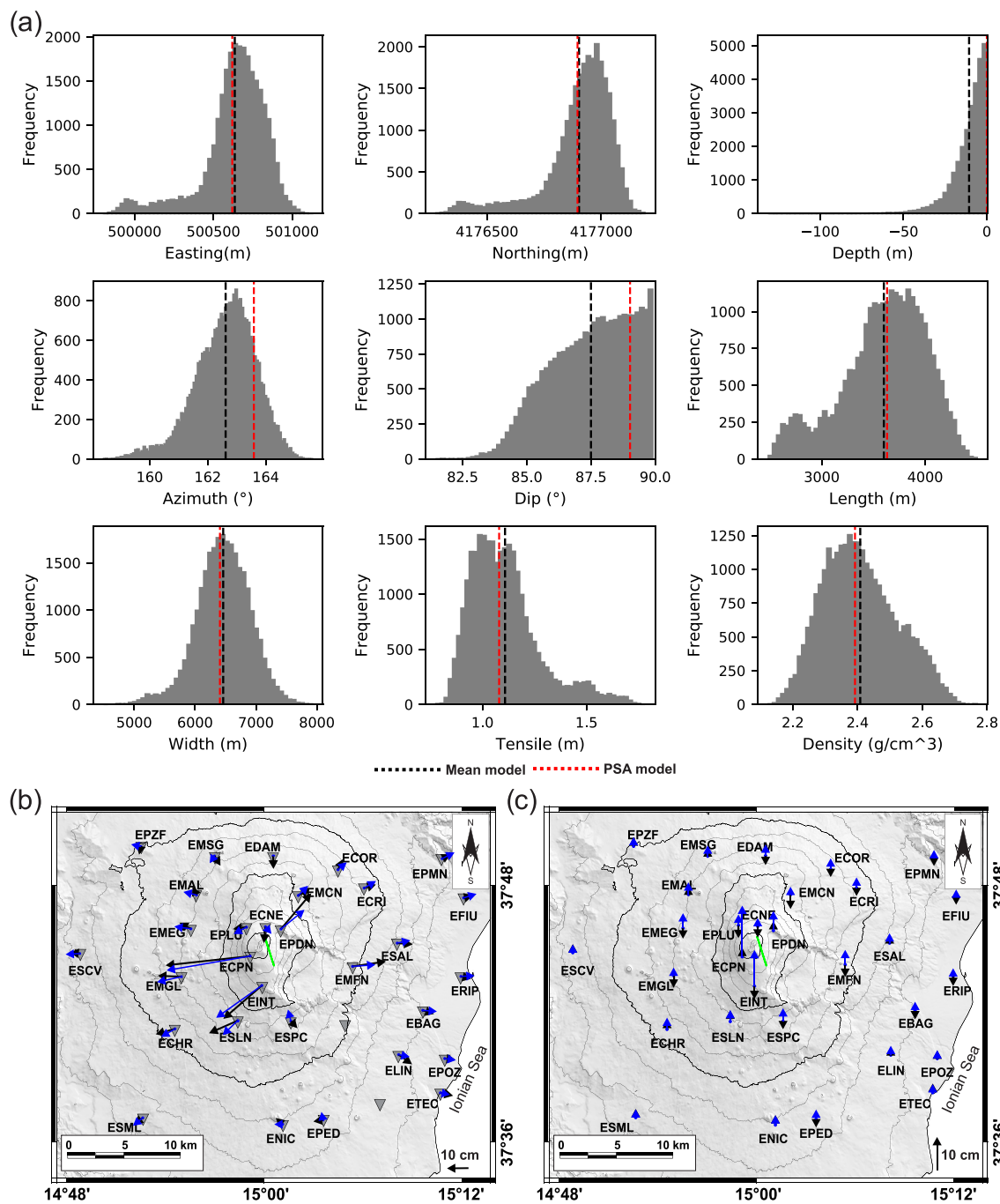


**Figure 3.** (a) Posterior density distribution of each model parameter, obtained using the Metropolis-Hastings sampler. As for depth (top of the dike), the distribution is with respect to the reference elevation (1,500 m). The black dotted lines represent the mean values, while the red dotted lines are the best fit values calculated by the Pattern Search Algorithm (PSA; line  $w_{III}$  in Table 1). (b) Observed (black arrows) and calculated (mean values obtained through the MCMC algorithm; blue arrows) horizontal deformation field. (c) Same as (b), but for the vertical component of the deformation field.

### 3.2. Posterior Probability Distribution of the Model Parameters

The Bayesian inversion of the GPS and gravity data set is performed following the method outlined in section 2. Figure 3a shows the estimated posterior probability density functions (PDFs) of the model parameters. There is, in general, a good agreement between inversion results obtained through PSA and MCMC methods (Table 1). The PDFs allow us to better understand the uncertainties associated with the

results and may expose possible weakness of the “best” model. For most parameters, an almost bell-shaped distribution with small variance indicates that the searched parameters are well constrained by the available data. Exceptions occur for depth and dip parameters, whose PDFs are skewed toward the edges of the searched ranges (0 m and 90°, respectively). This points to a relatively shallow and subvertical dike. The density PDF shows that, to explain the observations, this parameter must be lower than about 2.5 g/cm<sup>3</sup> with a probability of ~0.8.

### 3.3. Considerations on the Inversion Results

As shown in Figures 2a, 2b, 3b, and 3c, all the selected model sources allow us to obtain a very good fit to the horizontal component of the deformation field, while in the near field the models are not able to explain the observed vertical deformation. In particular, the models predict a marked uplift in the stations closer to the ground trace of the dike, while only minor vertical deformation (in some cases deflation) was observed at the GPS stations (Figures 2b and 3c). A first-order calculation, based on the semianalytical solutions of Williams and Wadge (2000), shows that the above discrepancy cannot be addressed by taking into account the possible effect of Etna’s topography on the near-field deformation.

While at SLN the iGrav SG and GPS receiver are only a few tens of meters apart, at MNT the iGrav sensor is not colocated with a GPS station (Figure 1). The GPS station closer to MNT is EINT; the two sites are about 500 m apart from each other. In the framework of the calculations described above, the elevation changes predicted by the Okada (1992) model at MNT are used in the Okubo (1992) formulation to retrieve the density of the intruding material. Indeed, the latter formulation predicts a marked uplift at the MNT site, implying that a large part of the gravity decrease observed at MNT is explained as due to the free-air effect of surface elevation. The GPS receiver at EINT recorded a very small elevation change (~1.55 cm) between 23 and 26 December 2018 (Figure 2b). Using DInSAR data, De Novellis et al. (2019) inferred a complex deformation pattern in a relatively small area surrounding the MNT site, with both inflation and deflation of several centimeters taking place across a distance of a few kilometers (Figure S2). It is thus difficult to be definitive about the magnitude of the elevation change that occurred at MNT during the studied interval. However, within the limits of the available data, both EINT and MNT stations fall in a zone where only minor vertical deformation is deduced from DInSAR measurements (Figure S2), in agreement with the GPS data from EINT. If an elevation change smaller than predicted by the Okada model is assumed for MNT and used as an input to the Okubo formulation, the free-air effect decreases and the negative density difference between host rock and lighter “intruding material” must increase accordingly, in order to fit the observed gravity changes. As shown in Figure S3, as the inflation assumed at MNT approaches negligible values, the density of the material inside the source body approaches values close to 0.

Another aspect that emerges from the results of the above calculations is the shallow position of the upper part of all the selected model structures. Indeed, the top of the best fitting dike is always aligned to the top of the considered elastic half-space (see Table 1). This observation highlights the limitations of analytical solutions based on the half-space approximation and suggests that a numerical approach, taking into account the prominent topography in the summit area of Etna (Beauducel & Carbone, 2015) and other relevant features (e.g., medium discontinuities), would be needed to get a more thoughtful insight into the processes that led to the breakout of the December 2018 eruption.

## 4. Discussion and Conclusion

In the present study, for the first time, gravity data from SGs are used jointly with ground deformation data, to shed new light on a paroxysmal volcanic event. Indeed, the high quality of continuous gravity data from SGs, in terms of both long-term stability and precision (Carbone et al., 2019), allows us to observe relatively small gravity changes (a few  $\mu$ Gal), without ambiguities about their development over time (negligible instrumental drift).

The December 2018 Etna eruption represents a peculiar paroxysmal event in different respects. The bulk of the eruption-related ground deformation pattern developed in a matter of hours (Cannavò et al., 2019; Figure 2d) and was driven by a ~1 m spreading of the volcano edifice and underlying sedimentary basement, across a depth range of some kilometers (Bonforte et al., 2019; De Novellis et al., 2019). Results of the present and previous studies indicate that the observed syneruptive deformation was associated to a

bulk volume increase of some tens of millions cubic meters (see Table 1; Bonforte et al., 2019; De Novellis et al., 2019), while the erupted volume (effusive activity) amounted to only  $1 \times 10^6 \text{ m}^3$ , or slightly more (Laiolo et al., 2019). Hence, the fast evolving and marked spreading of the volcano resulted in the emission of a relatively very small amount of lava. Moreover, the results of the analytical calculation we performed unanimously indicate a density of the intruding fluid lower than the typical magma density (see Table 1).

The feedback loop involving magma intrusion, seaward sliding of Etna's east flank (Urlaub et al., 2018) and tectonic forces (Carlino et al., 2019) may have led to the features observed in the geophysical data encompassing the December 2018 eruption. In particular, the Okada (1992) model, which accounts for the deformation effect arising from a tensile fault, allows matching the horizontal deformation but fails to explain the vertical component of the deformation field (Figures 2b and 3c). Indeed, a significant uplift is predicted by the Okada model in the area surrounding the trace of the dike model, while only minor vertical deformation (mostly deflation) was observed at the summit GPS stations (see section 3.3). Bonforte et al. (2019) explained this issue as due to depressurization of a deeper source, assumed to have supplied magma to the shallower levels of the plumbing system. However, it is unlikely that the transfer of some tens of millions cubic meters of magma may have occurred across a wide depth range (several km), over an interval of only a few hours (Aloisi et al., 2006; Armienti et al., 2012; Browne & Szramek, 2015). More likely, the complexity of the deformation field may reflect a partial inelastic accommodation of the strain, favored by the geodynamic framework of Etna. Accordingly, Murray (2019) suggested that phases of dike injection at Etna may induce subsidence and extension along a north-south graben-like structure in the summit of the volcano. Under this view, the mass decrease inferred through inversion of the gravity data could reflect an increase in the fracturing rate of the medium (Carbone et al., 2009, 2014), rather than indicating the intrusion of a light magma. Indeed, as shown in Figure S3, if the unlikely inflation of the MNT area, predicted by the Okada model, is neglected, a very low density of the intruding material must be considered in the Okubo formulation, which necessarily implies the creation of new void space in the shallower levels of the feeding fissure system. Regardless the limitations of the followed approach, we show that the joint analysis of deformation and gravity data can provide unique insight into the volcanic processes leading to paroxysmal phases of the activity, even if gravity data from only two sites are available. Indeed, the amplitude and sign of the observed gravity changes, together with the other evidences described above point to the conclusion that a more complex mechanism, likely involving the formation of new void space through local increase of the fracturing rate of the medium, rather than a mere dike injection, led to the breakout of the December 2018 eruption.

## Data Availability Statement

The data used in this research can be found in the Zenodo repository at the link (<https://zenodo.org/record/3695219#.Xl5HbqhKiUk>).

## Acknowledgments

The research was partially supported by the following projects: (1) INGV FISR 2017 OB.FU. 0893.010; (2) H2020 NEWTON-g project (Grant Agreement 801221). We thank the Editor Christian Huber and the reviewers F. Delgado and Mong-Han Huang for the critical reading of the manuscript. Their constructive comments helped us to significantly improve the manuscript.

## References

- Aloisi, M., Bonaccorso, A., & Gambino, S. (2006). Imaging composite dike propagation (Etna, 2002 case). *Journal of Geophysical Research*, 111, B06404. <https://doi.org/10.1029/2005JB003908>
- Alparone, S., Barberi, G., Giampiccolo, E., Maiolino, V., Mostaccio, A., Musumeci, C., et al. (2020). Seismological constraints on the 2018 Mt. Etna (Italy) flank eruption and implications for the flank dynamics of the volcano. *Terra Nova*, 1–11. <https://doi.org/10.1111/ter.12463>
- Altamimi, Z., Rebischung, P., Métivier, L., & Collilieux, X. (2016). ITRF2014: A new release of the international terrestrial reference frame modeling nonlinear station motions. *Journal of Geophysical Research: Solid Earth*, 121, 6109–6131. <https://doi.org/10.1002/2016JB013098>
- Amey, R. M. J., Hooper, A., & Walters, R. J. (2018). A Bayesian method for incorporating self-similarity into earthquake slip inversions. *Journal of Geophysical Research: Solid Earth*, 123, 6052–6071. <https://doi.org/10.1029/2017JB015316>
- Armienti, P., Perinelli, C., & Putirka, K. D. (2012). A new model to estimate deep-level magma ascent rates, with applications to Mt. Etna (Sicily, Italy). *Journal of Petrology*, 54(4), 795–813. <https://doi.org/10.1093/petrology/egs085>
- Audet, C., & Dennis, J. E. (2002). Analysis of generalized pattern searches. *SIAM Journal on Optimization*, 13(3), 889–903. <https://doi.org/10.1137/s1052623400378742>
- Bagnardi, M., & Hooper, A. (2018). Inversion of surface deformation data for rapid estimates of source parameters and uncertainties: A Bayesian approach. *Geochemistry, Geophysics, Geosystems*, 19, 2194–2211. <https://doi.org/10.1029/2018gc007585>
- Beauducel, F., & Carbone, D. (2015). A strategy to explore the topography-driven distortions in the tilt field induced by a spherical pressure source: The case of Mt Etna. *Geophysical Journal International*, 201(3), 1471–1481. <https://doi.org/10.1093/gji/ggv076>
- Bonforte, A., Guglielmino, F., & Puglisi, G. (2019). Large dyke intrusion and small eruption: The December 24, 2018 Mt. Etna eruption imaged by Sentinel-1 data. *Terra Nova*, 31, 405–412. <https://doi.org/10.1111/ter.12403>
- Browne, B., & Szramek, L. (2015). Chapter 9 – Rates of magma ascent and storage. In H. Sigurdsson (Ed.), *The Encyclopedia of Volcanoes* (2nd ed., pp. 203–214). Amsterdam: Academic Press. <https://doi.org/10.1016/B978-0-12-385938-9.00009-2>

- Bruno, V., Mattia, M., Aloisi, M., Palano, M., Cannavò, F., & Holt, W. E. (2012). Ground deformations and volcanic processes as imaged by CGPS data at Mt. Etna (Italy) between 2003 and 2008. *Journal of Geophysical Research*, 117, B07208. <https://doi.org/10.1029/2011JB009114>
- Calvari, S., Bilotta, G., Bonacorso, A., Caltabiano, T., Cappello, A., Corradino, C., et al. (2020). The VEI 2 Christmas 2018 Etna eruption: A small but intense eruptive event or the starting phase of a larger one? *Remote Sensing*, 12(6), 905. <https://doi.org/10.3390/rs12060905>
- Cannavò, F. (2019). A new user-friendly tool for rapid modelling of ground deformation. *Computers & Geosciences*, 128, 60–69. <https://doi.org/10.1016/j.cageo.2019.04.002>
- Cannavò, F., Cannata, A., Cassisi, C., Grazia, G. D., Montalto, P., Prestifilippo, M., et al. (2017). A multivariate probabilistic graphical model for real-time volcano monitoring on Mount Etna. *Journal of Geophysical Research: Solid Earth*, 122, 3480–3496. <https://doi.org/10.1002/2016JB013512>
- Cannavò, F., Sciotto, M., Cannata, A., & Grazia, G. D. (2019). An integrated geophysical approach to track magma intrusion: The 2018 christmas eve eruption at Mount Etna. *Geophysical Research Letters*, 46, 8009–8017. <https://doi.org/10.1029/2019GL083120>
- Carbone, D., Aloisi, M., Vinciguerra, S., & Puglisi, G. (2014). Stress, strain and mass changes at Mt. Etna during the period between the 1991–93 and 2001 flank eruptions. *Earth-Science Reviews*, 138, 454–468. <https://doi.org/10.1016/j.earscirev.2014.07.004>
- Carbone, D., Cannavò, F., Greco, F., Reineman, R., & Warburton, R. J. (2019). The benefits of using a network of superconducting gravimeter to monitor and study active volcanoes. *Journal of Geophysical Research: Solid Earth*, 124, 4035–4050. <https://doi.org/10.1029/2018JB017204>
- Carbone, D., D'Amico, S., Musumeci, C., & Greco, F. (2009). Comparison between the 1994–2006 seismic and gravity data from Mt. Etna: New insight into the long-term behavior of a complex volcano. *Earth and Planetary Science Letters*, 279(3–4), 282–292. <https://doi.org/10.1016/j.epsl.2009.01.007>
- Carbone, D., Poland, M. P., Diament, M., & Greco, F. (2017). The added value of time-variable microgravimetry to the understanding of how volcanoes work. *Earth-Science Reviews*, 169, 146–179. <https://doi.org/10.1016/j.earscirev.2017.04.014>
- Carlino, M. F., Cavallaro, D., Coltellini, M., Cocchi, L., Zgur, F., & Patanè, D. (2019). Time and space scattered volcanism of Mt. Etna driven by strike-slip tectonics. *Scientific Reports*, 9(1), 12,125. <https://doi.org/10.1038/s41598-019-48550-1>
- De Novellis, V., Atzori, S., Luca, C. D., Manzo, M., Valerio, E., Bonano, M., et al. (2019). DInSAR analysis and analytical modeling of Mount Etna displacements: The December 2018 volcano-tectonic crisis. *Geophysical Research Letters*, 46, 5817–5827. <https://doi.org/10.1029/2019GL082467>
- Di Grazia, G., Cannata, A., Montalto, P., Patanè, D., Privitera, E., Zuccarello, L., & Boschi, E. (2009). A multiparameter approach to volcano monitoring based on 4d analyses of seismo-volcanic and acoustic signals: The 2008 Mt. Etna eruption. *Geophysical Research Letters*, 36, L18307. <https://doi.org/10.1029/2009GL039567>
- Dong, D., Herring, T. A., & King, R. W. (1998). Estimating regional deformation from a combination of space and terrestrial geodetic data. *Journal of Geodesy*, 72(4), 200–214. <https://doi.org/10.1007/s001900050161>
- Hastings, W. K. (1970). Monte Carlo sampling methods using Markov chains and their applications. *Biometrika*, 57(1), 97–109. <https://doi.org/10.1093/biomet/57.1.97>
- Herring, T. A., King, R. W., & McClusky, S. C. (2010). Introduction to GAMIT/GLOBK, release 10.4. Massachusetts Institute of Technology, Cambridge.
- King, R. W., & Bock, Y. (2004). Documentation of the MIT GPS analysis software: GAMIT, release 10.2, user's manual. Massachusetts Institute of Technology, Cambridge.
- Laiolo, M., Ripepe, M., Cigolini, C., Coppola, D., Schiava, M. D., Genco, R., et al. (2019). Space and ground-based geophysical data tracking of magma migration in shallow feeding system of Mount Etna volcano. *Remote Sensing*, 11(10), 1182. <https://doi.org/10.3390/rs11101182>
- Minson, S. E., Simons, M., & Beck, J. L. (2013). Bayesian inversion for finite fault earthquake source models I—Theory and algorithm. *Geophysical Journal International*, 194(3), 1701–1726. <https://doi.org/10.1093/gji/gjt180>
- Mosegaard, K., & Tarantola, A. (1995). Monte carlo sampling of solutions to inverse problems. *Journal of Geophysical Research*, 100(B7), 12,431–12,447. <https://doi.org/10.1029/94JB03097>
- Murray, J. B. (2019). The cryptic summit graben of Mt. Etna volcano. *Journal of Volcanology and Geothermal Research*, 387, 106657. <https://doi.org/10.1016/j.jvolgeores.2019.07.024>
- Okada, Y. (1992). Internal deformation due to shear and tensile faults in a half-space. *Bulletin of the Seismological Society of America*, 82(2), 1018–1040.
- Okubo, S. (1992). Gravity and potential changes due to shear and tensile faults in a half-space. *Journal of Geophysical Research*, 97(B5), 7137. <https://doi.org/10.1029/92JB00178>
- Palano, M., Rossi, M., Cannavò, F., Bruno, V., Aloisi, M., Pellegrino, D., et al. (2010). Etn@ref: A geodetic reference frame for Mt. Etna GPS networks. *Annals of Geophysics*, 53(4), 49–57. <https://doi.org/10.4401/ag-4879>
- Palano, M., Viccaro, M., Zuccarello, F., & Gresta, S. (2017). Magma transport and storage at Mt. Etna (Italy): A review of geodetic and petrological data for the 2002–03, 2004 and 2006 eruptions. *Journal of Volcanology and Geothermal Research*, 347, 149–164. <https://doi.org/10.1016/j.jvolgeores.2017.09.009>
- Sen, M. K., & Stoffa, P. L. (1996). Bayesian inference, Gibbs sampler and uncertainty estimation in geophysical inversion. *Geophysical Prospecting*, 44(2), 313–350. <https://doi.org/10.1111/j.1365-2478.1996.tb00152.x>
- Tarantola, A. (1984). Inversion of seismic reflection data in the acoustic approximation. *Geophysics*, 49(8), 1259–1266. <https://doi.org/10.1190/1.1441754>
- Tarantola, A., & Valette, B. (1982). Generalized nonlinear inverse problems solved using the least squares criterion. *Reviews of Geophysics*, 20(2), 219. <https://doi.org/10.1029/rg020i002p00219>
- Urlaub, M., Petersen, F., Gross, F., Bonforte, A., Puglisi, G., Guglielmino, F., et al. (2018). Gravitational collapse of Mount Etna's south-eastern flank. *Science Advances*, 4(10), eaat9700. <https://doi.org/10.1126/sciadv.aat9700>
- Warburton, R. L., Pillai, H., & Reineman, R. C. (2010). Initial results with the new GWR iGrav superconducting gravity meter. In *Paper Presented at: IAG Symposium on Terrestrial Gravimetry: Static and Mobile Measurements (TGSMM2010)*, Saint Petersburg, Russia.
- Williams, C. A., & Wade, G. (2000). An accurate and efficient method for including the effects of topography in three-dimensional elastic models of ground deformation with applications to radar interferometry. *Journal of Geophysical Research*, 105(B4), 8103–8120. <https://doi.org/10.1029/1999JB900307>